Understanding of water uptake mechanisms in an epoxy joint characterized by pore-type defects

Andreea Tintatu, C. Badulescu, Pierre Bidaud, Philippe Le Grognec, Jérôme Adrien, E Maire, Hervé Bindi, Corentin Coguenanff

Understanding of water uptake mechanisms in an epoxy joint characterized by pore-type defects

A. Tintatu[1], C. Badulescu[1], P. Bidaud[1], P. Le Grognec[1,*], J. Adrien[2], E. Maire[2], H. Bindi[3], C. Coguenanff[3]

[1] *ENSTA Bretagne, UMR CNRS 6027, IRDL, F-29200, Brest, France*

[2] *Univ. Lyon, INSA Lyon, UMR CNRS 5510, Laboratoire MATEIS, F-69621, Villeurbanne Cedex, France*

[3] *Thalès DMS France, 525 route des Dolines, 06560, Valbonne, France*

* Corresponding author:
Pr. Philippe Le Grognec
Institut de Recherche Dupuy de Lôme
ENSTA Bretagne
2 rue François Verny
29806 Brest Cedex 9, FRANCE
Phone: +33.(0)2.98.34.88.67 Fax: +33.(0)2.98.34.87.30
Email: philippe.le_grognec@ensta-bretagne.fr

Understanding of water uptake mechanisms in an epoxy joint characterized by pore-type defects

This work aims to characterize the water uptake mechanisms of a two-component epoxy adhesive joint immersed in deionized water. The pore-type defects in the bulk adhesive after the cure cycle are highlighted and characterized using X-ray µ-tomography. Two population patterns of defects are generated and analyzed, for two different thicknesses. The waterfront is not detectable by µ-tomography for this adhesive because the densities of the water and the adhesive remain relatively close to each other. Instead, the volume variation and kinetics of pore water filling have been accurately identified. This analysis was completed by optical observations and gravimetric measurements.

Keywords: structural bonding, water aging, X-ray µ-tomography, pores

1. Introduction

The complexity and efficiency of underwater systems including composite structures and multi-material watertight assemblies must be constantly increasing, showing long-range, real-time investigation capabilities. The constitution of such complex systems passes by a phase of assembly of various subsystems. Although most structures can be assembled by screws or riveting systems [1], adhesive bonding is becoming an increasingly attractive alternative, due to its numerous advantages: (i) lightweight, (ii) more uniform load distribution, (iii) ease of implementation, and (iv) possibility of joining different materials (metal with composite) [2]. The structural mechanical resistance as well as the durability of bonded structures are closely related to the degradation mechanisms to be integrated in the dimensioning stage. In structural assemblies, epoxy adhesives are most often used because they are characterized by a relatively high mechanical resistance to failure, allowing them to reach load levels close to those that the primary structure supports. Nevertheless, these adhesives require careful characterization of their thermo-mechanical behavior so as to correctly predict

the long-term mechanical response of the assembly. Additional complexity is experienced if the mechanical behavior of the adhesive is influenced by the humidity of the water environment that diffuses into the material.

The influence of water on the mechanical behavior of adhesives is a widely studied topic [3-5]. The phenomenon of aging of an adhesive, when water diffuses into it, is manifested by a loss of its mechanical properties. Also, humidity could lead to a degradation of the assembly interface, an aspect that is not addressed in this paper. Generally, the studies investigating the effect of water on the mechanical behavior of an assembly may be very costly in terms of time and experimental means deployed. When possible, accelerated aging investigations are a good alternative, remedying to these difficulties. In the context of accelerated aging, bulk adhesive samples drastically reduce the time required to obtain a uniform humidity inside the material, due to the very large contact surface between the wet medium and the adhesive. Moreover, the increase of the temperature of the hydrous environment used to age the samples (immersion in water or humid atmosphere controlled at a certain percentage of RH) drastically decreases (from months to weeks) the time necessary for the samples to reach the water saturation. This accelerated aging strategy has already been successfully applied to several adhesives, confirming its relevance [3]. However, phenomena such as the physical aging of adhesives cannot be observed over short durations associated with rapid investigation strategies.

Many authors agree that the sorption of water by polymeric materials, such as epoxy adhesives, causes a weakening of the mechanical properties and also a swelling of the samples [6]. These swelling changes are relatively small and difficult to measure by conventional means. In previous works [7,8], the authors proposed an experimental strategy to measure the moisture in an adhesive using a fiber optic sensor (Bragg or

Fresnel). However, this method of investigation is intrusive and, considering the diameter of the fibers, this approach is not suitable for thin adhesive joints (with thicknesses less than 1 mm). Direct experimental measurements of the percentage of water in an adhesive are difficult to perform and, in the few cases where it is possible (using Neutron Radiography, for example), it is necessary to deploy very sophisticated means and methods of investigation [9]. A potential technique to determine the moisture gradient in a joint is represented by X-ray µ-tomography. This technique has been successfully used in several studies [10,11], mainly for the detection of the advancement of the moisture front in concrete or other civil engineering structures. Recently, Dumont *et al.* [12] also used X-ray µ-tomography successfully to identify, at the micrometric scale, the pore-type defects present in an adhesive joint and their evolution depending on the mechanical loading.

The objective of this paper is to investigate by X-ray µ-tomography the mechanisms of water uptake within a structural bi-component epoxy adhesive. More precisely, the aim is to understand the mechanisms of water linked to the water uptake during hydric aging, but also to study the influence of pore-type defects on global sorption. These investigations are completed by gravimetric measurements and optical observations in order to better understand the mechanisms that govern the absorption of water in such an adhesive. The paper is organized in two main sections. In Section 2, the adhesive material is described, and the different methods used to investigate its water uptake are presented. Section 3 displays then the results of the tomographic analyses performed directly after curing and at different aging times, so as to highlight the changes in the microstructure due to water uptake. These results are finally correlated with classical gravimetric measurements and confronted to microscopic observations.

2. Material and experimental methods

2.1. Sample preparation

The nature and characteristics of the samples used must be carefully selected, depending on the final application. The main objective of the overall project in hand is to understand, characterize and model the water uptake and its effect on the mechanical behavior of a bonded assembly (such as between a composite material and a polyurethane, but not only). The adhesive thickness within the assembly is supposed to vary between 300 µm and 500 µm. Such an assembly is designed to remain immersed in seawater for long periods of time. Owing to the low mechanical load that this adhesive joint must withstand, one will mainly focus on the degradation of the mechanical properties caused by water absorption.

The specimens used in this study are bulk samples made of an epoxy-based adhesive with a bisphenol A diglycidyl ether prepolymer and a diamine hardener mixed under stoichiometric conditions. Table 1 summarizes some main properties of this material.

The two components of the adhesive were mixed according to the manufacturer's specifications in the following proportions: 100 parts by weight of resin A and 40 parts by weight of hardener B, using a Speedmixer planetary mixer (FlackTek Inc., Landrum, USA). The mixing parameters correspond to a rotation speed of 2500 rpm during 4 minutes. With this type of adhesive, it has been observed that the mixing process was prone to generate porosities inside the material [13]. This mixture was then cast between two aluminum plates, each 300 × 300 × 30 mm^3 in size. These plates were wrapped in a Teflon film, in order to avoid the adhesion of the adhesive material once it has cured. The distance between these two plates is controlled with calibrated spacers, so as to obtain the desired adhesive thicknesses. Two adhesive plates were finally made

with two different thicknesses, namely 0.4 mm and 1 mm. A third plate, with a thickness of 0.4 mm, was made by vacuuming the adhesive mixture during 5 minutes before pouring it in the apparatus, for further comparison purposes.

Table 1. Main characteristics of the considered adhesive

Property	*Component A*	*Component B*	Mix
Density	1,2 g/cm³	1,0 g/cm³	∼ 1,07 g/cm³
Glass transition temperature (DSC)			∼ 55°C
Young modulus			1700 MPa
Known fillers			Glass beads

The curing cycle used for the three types of samples was set at 50°C for 12 hours. It was performed using a MEMERT UF110+ thermal chamber which allows the temperature to vary between 20°C and 310°C. The density of the adhesive was determined to be equal to 1087 kg/m^3. DSC analyses have shown that this curing process ensures a polymerization rate of 95%. Several samples were then taken from the three adhesive thin plates, respectively named E1-1mm-P1, E2-0.4mm-P1 and E3-0.4mm-P2. In this paper, for clarity purposes, they will be referred to as E1, E2 and E3, respectively.

First, three samples of size 30 × 30 mm^2 for each of the three plates were cut as shown in Figure 1a, using a waterjet cutting machine. These dimensions are chosen following the recommendations proposed by previous studies [3], in order to ensure unidirectional (through-the-thickness) patterns while minimizing edge effects, which could have a non-negligible influence for small sample sizes. These first specimens were used for gravimetric analyses.

Thereafter, samples of size 25 × 6 mm^2, taken from each sheet (A, B and C), were put together in a holder, as shown in Figure 1b. The interest in placing together these last three samples is to decrease the tomographic analysis time. In other words,

with such a configuration, a single tomographic scan allows one to obtain the results for the three samples simultaneously.

Samples E1, E2 and E3 were obtained for a curing cycle (12h @ 50°C) by varying two parameters: (i) thickness and (ii) porosity ratio, as presented above. For a better understanding of the effect of water uptake in the samples and the influence of thickness and porosity ratio, the study is focused on two investigations: classical water absorption by gravimetric measurements on immersed samples, and analysis by X-ray tomography. For efficiency reasons and coherence with the availability of experimental means, the temperature of aging was established at 22°C.

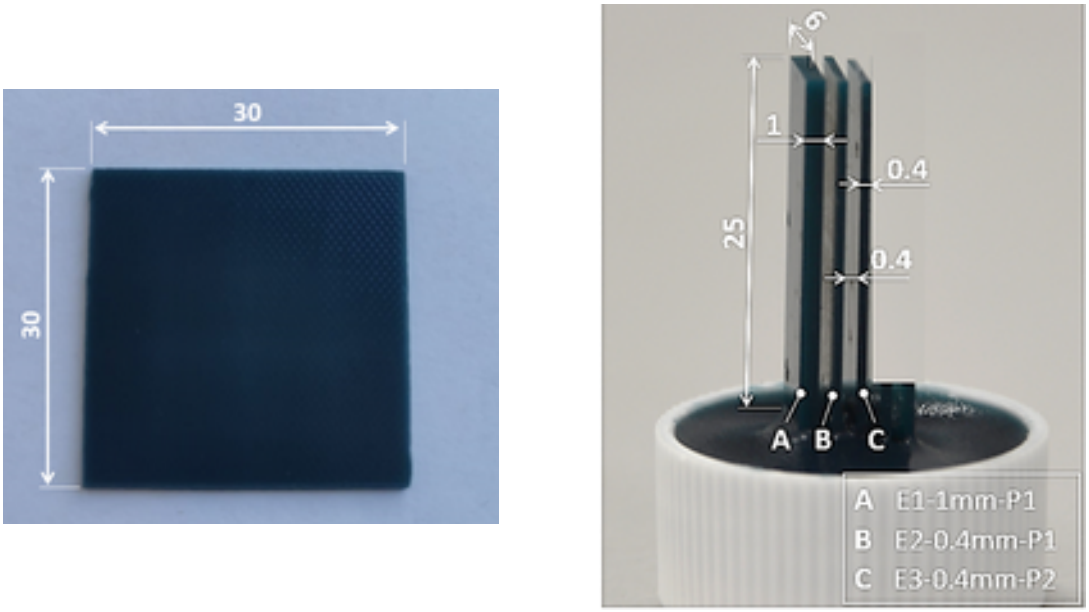

a) Sample for classical gravimetry investigation (1 mm thickness)

b) Samples for X-ray tomography investigation

Figure 1. Geometry of the samples (dimensions in mm)

2.2. Optical microscopy

Experimental observations were performed using the KEYENCE VHX-7000 3D microscope. The corresponding samples, 30 x 30 x 0.4 mm^3 in size, were investigated using the through illumination system, with which the observation device is equipped.

The aim here is to observe qualitatively the porosity distribution but also the time needed for the first water droplets to occur in the pores of the samples.

2.3. Global water uptake

The three samples of size 30 × 30 mm^2 (collected from each plate) were first dried in order to remove residual moisture. The presence of moisture in the samples can be explained first by the absence of moisture control during the curing cycle, but also by the contact of the samples with water, during the cutting operation. This drying phase was carried out by placing the samples in a glass container with Silica gel at 35°C. Periodic measurements of mass decrease were performed to determine the necessary time for mass stabilization. Twenty-one days were needed to reach a quasi-dry state of the samples. These dried samples were then immersed in demineralized water for practical reasons (manufacturing and water control). Deroiné *et al.* [14] have also shown that water diffusion kinetics are slightly faster in demineralized water. The density of demineralized water is 1020 kg/m^3. The aging tanks containing the demineralized water, at a temperature of 22°C +/- 0.3°C, are equipped with a water circulation system, responsible for the homogenization of the temperature in the whole water mass. Weight measurements were periodically performed during 4 months. These measurements were carried out with a more important frequency at the beginning of the water uptake (every 12 hours for the first three days) and a less important one thereafter. Water diffusion was determined from the change in weight of the square samples. Samples were removed from the aging tanks and wiped before weighing. The mass increase was followed by periodic weighing on a Kern AEJ 200-4CM balance with an accuracy of 0.0001 g.

2.4. X-ray tomography

Since its first applications in the medical field [15], X-ray tomography has been the subject of numerous studies from both a theoretical and applied point of view. A brief description is therefore given here to introduce the main concepts. A wide variety of experimental setups can be used to perform X-ray tomography, but the basic principles of the technique always remain the same (see Figure 2). Tomography measurements are based on the variation of the linear X-ray attenuation coefficient, denoted μ, through the volume of a material. For a material considered as homogeneous, the coefficient μ turns out to be constant with respect to the spatial coordinates (x, y, z). Conversely, in heterogeneous materials such as porous environments, μ is a function of these coordinates.

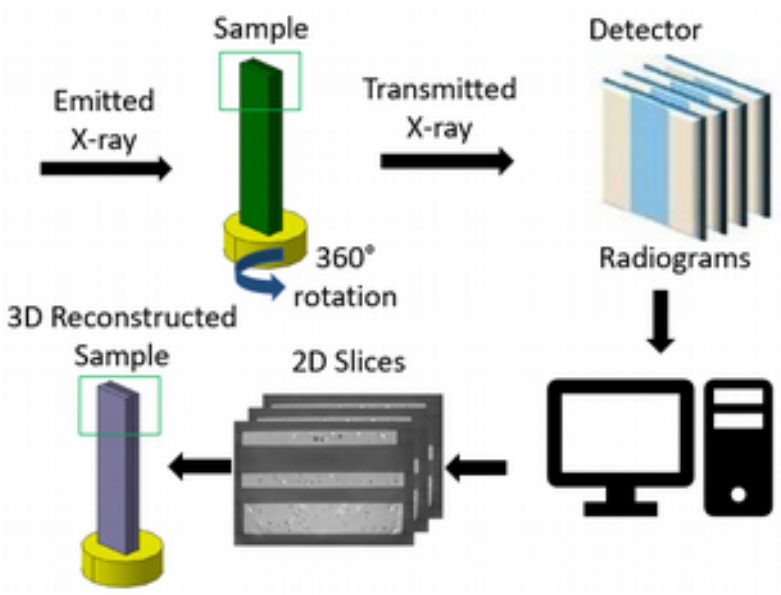

Figure 2. Principle of tomography measurements

It is possible to obtain the spatial distribution of this coefficient μ by sending a beam of X-rays into the mass of the studied sample, under different angles, and by collecting the transmitted beam. In practice, the sample is mounted on a rotator included

in the tomograph chamber, and for each angular step, an X-ray beam is emitted, attenuated by the internal structure of the sample, and collected by a detector. The attenuation phenomenon in the $\vec{x}$ direction is described by a Beer-Lambert law depending on $\mu(x,y,z)$:

$$\frac{I}{I_0} = \exp\left(\int_{x_0}^{x_{max}} \mu(x, y, z) dx \right) \quad (1)$$

where I_0 represents the initial intensity of the source (emitted), I is the detected intensity (transmitted and collected by the X-ray detector) and x represents the distance along the transmission path between x_0 and x_{max}.

A series of N radiographs is obtained by the complete acquisition process. A reconstruction algorithm is then used to generate the 3D internal structure of the sample (i.e. the spatial distribution of $\mu(x, y, z)$) from the series of radiographs. This algorithm can be based on two different approaches: the software can either solve a set of linear equations to compute $\mu(x, y, z)$ (algebraic approach) or use a back-projection of the detected intensity by a Fourier transformation (analytical approach). Although the analytical approach is faster to compute, it requires a complete data set with no missing pictures of the X-ray series.

The results presented in this paper were obtained using a filtered back-projection approach. The X-ray computed tomography equipment (model Phoenix vTomeX / X-ray, see 3) that is used during this experimental study is located in the MATEIS laboratory (INSA Lyon, France). The tomograph is equipped with a *Varian Paxscan*™ flat-panel detector with a resolution of 1920 × 1536 pixels^2. This detector produces 14-bit coded grayscale pictures of the attenuation.

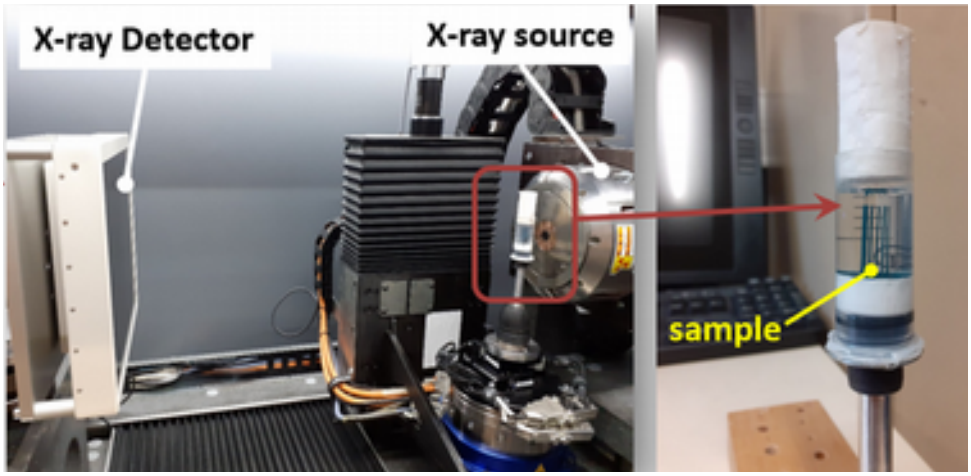

Figure 3. X-ray computed tomography equipment, model Phoenix vTomeX (MATEIS / INSA Lyon)

The acquisition was performed with a rotational movement of the sample in order to reconstitute all the investigated volume. A total of 1200 pictures were taken throughout the rotation, for a complete acquisition time of 15 min. The X-ray source was operated with a voltage of 60 kV and a current of 80 µA. These values are chosen so as to ensure the best compromise between transmission and contrast. Concerning the current, the maximum value (before defocusing) is used in order to obtain the maximum photon flux without increasing the size of the source spot.

In parallel to the measurements of mass changes, measurements of X-ray µ-tomography were made periodically with a similar frequency to the previous tests. The samples used are shown in Figure 1b. Only the upper part of these samples is analyzed, namely a volume of 6 × 6 × 6 mm^3 as described in Figure 2. Under these conditions, a voxel of 4.5 × 4.5 × 4.5 $µm^3$ is obtained. The samples were placed in a cylindrical container made of transparent plastic material. This container, filled with demineralized water, ensures the immersion of the sample and significantly facilitates the execution of the tests. The samples are positioned centrally and then fixed to a metal rod as shown in

Figure 3. The purpose of the rod is to ensure an almost identical positioning between the X-ray tube and the specimen, during the acquisition of the various radiograms, and thus to facilitate the setting up of the acquisition.

3. Results and discussions

3.1. Preliminary observation of the samples by optical microscopy

In Figure 4, two images of two samples E1 and E3, both with a thickness of 0.4 mm, are depicted. These images were obtained with the KEYENCE VHX-7000 microscope with an illumination of the sample by the bottom side. When the sample is semi-transparent and not too thick, this illumination serves to highlight the different phases within the samples. The presence of porosities after curing can be qualitatively observed in Figure 4a, in the form of dark small spheres, which are characterized by a relatively uniform distribution. Regular white dots are also detected, which represent glass beads. Figure 4b illustrates the microscopic image of a sample E3. In this case, the adhesive mixture has been put under vacuum during 5 minutes (before the process of curing) and then immersed into water during 30 days. The vacuum effect clearly appears through the absence of small porosities and the presence of very large ones (these large pores could have further a significant influence on the long-term mechanical strength of the adhesive). What is remarkable is that keeping the adhesive in a viscous state under vacuum cannot completely eliminate the presence of porosities. Moreover, from 21 days of immersion, the first water droplets appeared inside the largest porosities closest to the two faces of the sample. Water-filled porosities positioned in the vicinity of the adhesive-substrate interface in assemblies may also accelerate local degradation of the interface with significant consequences for the integrity of the structure.

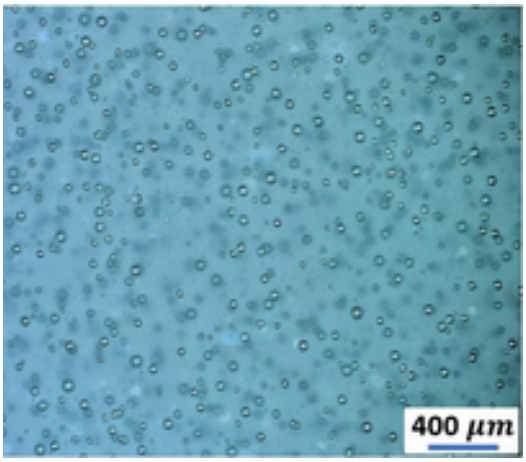

a) Sample E1 (0.4 mm thick) after curing

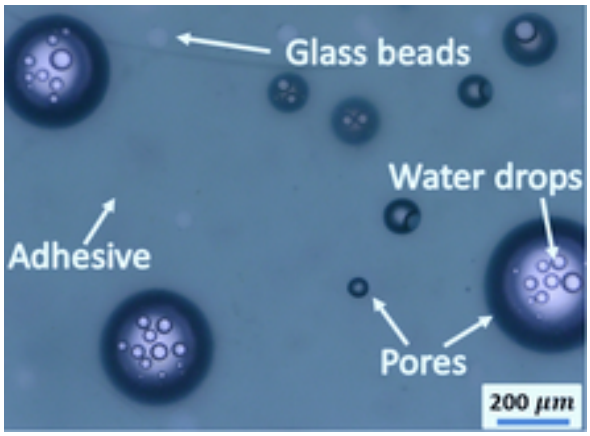

b) Sample E3 (0.4 mm thick) after 1 month in demineralized water

Figure 4. Different types of porosities observed by microscope within the samples obtained from the two mixtures

Although these observations are only qualitative, they give an insight of the mechanisms of water absorption in the adhesive, e.g. the migration of water through the material to the pores so as to occupy the free volumes. The kinetics of such a mechanism will clearly be influenced by the distribution and size of the porosities.

As these preliminary observations remain qualitative, analyses by X-ray µ-tomography were carried out in order to understand more deeply these mechanisms in a quantitative and local way. The interest is to investigate whether it is possible to determine the concentration profile of water in the adhesive during aging. Mass change measurements were performed in parallel so as to complete these observations.

3.2. Global water uptake

The purpose of gravimetric tests is to determine the kinetics of water uptake in adhesive samples. These macroscopic measurements will complement tomographic investigations. The mass change measurements were performed on square-shaped samples, as presented in Section 2.1. Regarding the sample dimensions used, the assumption of a unidirectional diffusion is made. The temperature of water has been set

to 22°C. Nine samples per condition were used with three measurements at each time. Specimens were dried with lint-free tissue before recording the final weight. The water uptake was determined by gravimetric measurements. The mass water content in the adhesive can be calculated from:

$$C(t)=\frac{m(t)-m_0}{m_0}\times 100 \tag{2}$$

where $m(t)$ and m_0 represent the mass of the adhesive during immersion and the initial mass, respectively. The water uptake results for the three sample types are plotted in Figure 5.

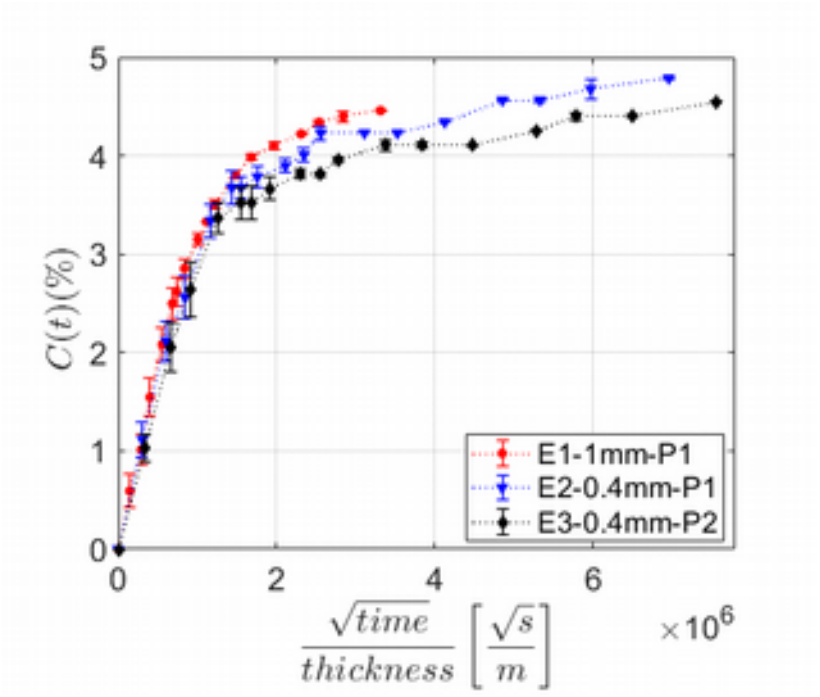

Figure 5. Water uptake of the three samples during immersion

In the present case of unidirectional diffusion, the evolution of the mass water content $C(t)$ can be classically represented as a function of the square root of time. It allows one to identify a first linear part in the sorption kinetics. Furthermore, the linear growth in the second part instead of a plateau suggests a non-Fickian water uptake kinetics for the adhesive in hand. All the results were normalized with respect to the

thickness, so as to be free from thickness effects, while considering sufficiently thin samples in such a way that water diffusion remains unidirectional.

3.3. X-ray tomography and image analysis

3.3.1. Configuration choice

The quality of the tomographic measurements is a key point for obtaining reliable results. For the scale being considered, three phases are supposed to be determined in the adhesive composition: the polymeric medium (adhesive phase), the glass beads and the pores, as shown in Figure 4. The measurement parameters of the tomograph have been selected in order to detect at best these three phases in a robust manner.

Regarding now the scanning investigations performed, two configurations were considered: (i) samples immersed in water and (ii) samples without water in the container. The first configuration avoids water desorption during the 15 minutes of scanning. It also eliminates some artifacts occurring at the interface between the glass beads and the adhesive phase, as shown in Figure 6b (see the blue ellipses). However, in this configuration, it is no longer possible to distinguish the edges of the sample, which further complicates the analysis of each volume. Also, the water that penetrates the pores cannot be separately identified. Moreover, the measurement noise is more important in this configuration. Conversely, the second configuration allows the separation of the ambient air surrounding the volumes and the measurement of their variation. Gravimetric analyses were also performed so as to determine the loss of mass of the samples in configuration (ii). These measurements showed that about 0.15% of the mass is lost in 15 minutes if the sample is in ambient air at the temperature of 22°C and a humidity of 75% RH. This desorption phenomenon could therefore be considered as negligible, when compared to the long-term water uptake.

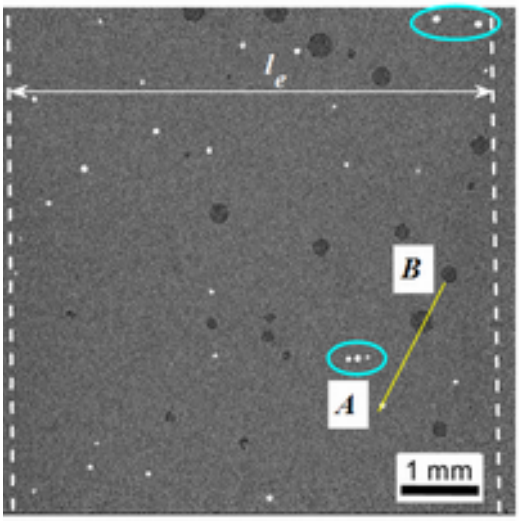

a) Slice of sample E3 scanned when surrounded by water

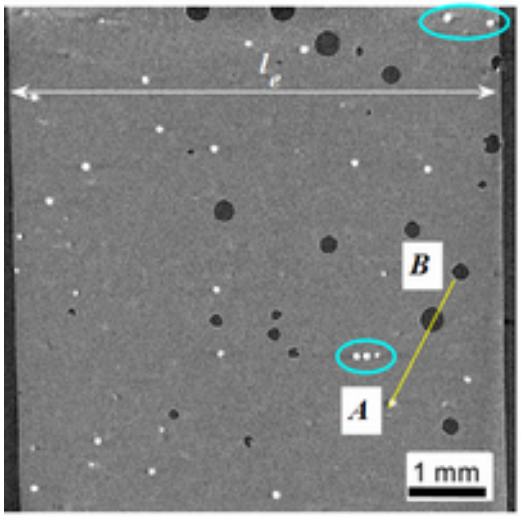

b) Section in the middle of sample E3 scanned when not submerged in water (l_e represents the width of the sample equal to 6 mm at the initial state)

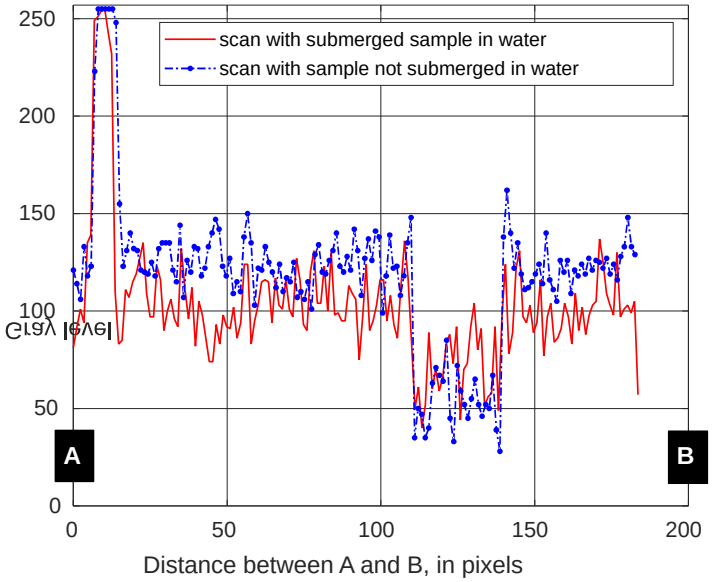

c) Gray level comparison between the two configurations on the same AB path

Figure 6. Two configurations of tomographic analyses

Figure 6c shows an overlay of the gray levels along the AB path (which is represented with a yellow line in Figure 6a and Figure 6b for both configurations. It can be observed that the measurement noise decreases slightly for the configuration (ii). On top of that, the pore contrast increases, which facilitates the segmentation step of the different pores with fewer errors. Based on these preliminary investigations, it can then

be justified that configuration (ii) provides more advantages than configuration (i). Nevertheless, it is important to note that a systematic loss of mass could explain some discrepancies in the comparison between the gravimetric measurements and the tomographic observations.

3.3.2. Image analysis

In order to make the best use of data arising from the reconstructed volumes, it is necessary to perform segmentation so as to isolate properly the different phases. This is a common concern in the field of image processing and computer vision, and it has been the subject of many studies, which have proposed a wide variety of methodologies [16].

The simplest way to segment grayscale data with multiple phases is based on thresholding segmentation. Even if this method is rather basic, it generally provides satisfactory results, taking into account that the histogram of the data is adequate (i.e. the phases are easily distinguishable). The threshold can be chosen manually or calculated algorithmically; the latter being often preferred. The numerical determination of the threshold can be achieved in different ways: it can be based on the analysis of the histogram [17], or by grouping the grayscale levels [18], for example. More details concerning such methods are presented in [19].

The processing strategy adopted in this study, dedicated to the segmentation of the three phases in hand, is described in the sequel. First, the reconstructed volume, represented by the red parallelepiped in Figure 7a, takes the following dimensions of 6.5 × 6 × 5 mm^3. This volume, initially coded on 14 bits, is converted to 8 bits in order to facilitate data exploitation on conventional computers. The coding depth degradation affects insignificantly the phase segmentation. The three volumes of each sample are then separated as shown in Figure 7b, using the Fiji software [20]. Some artifacts are visible around glass beads for sample E1. In Figure 7c and Figure 7d, a section in the *xy*

plane at half thickness is shown for samples E1 and E3, respectively. In these two figures, the porosities, the glass beads and the adhesive phase as well as their distribution are clearly visible.

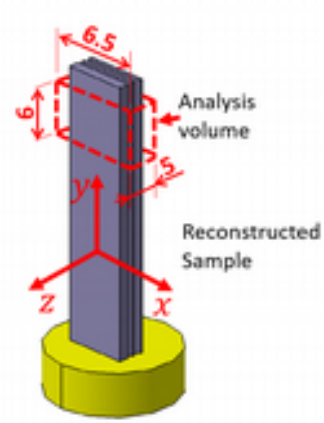

a) Samples and volume investigated by X-ray µ-tomography (dimensions in mm)

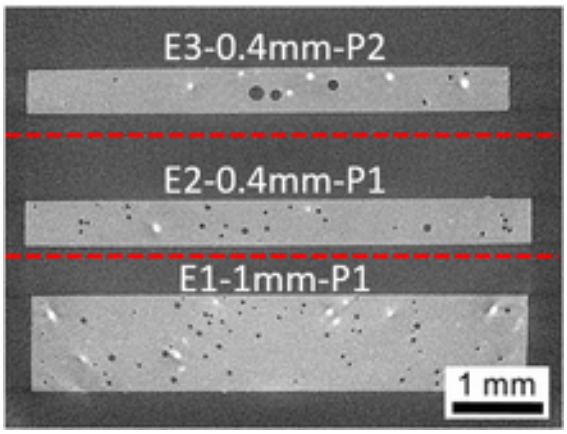

b) Section in the *x z* plane of the reconstructed volume of the three samples

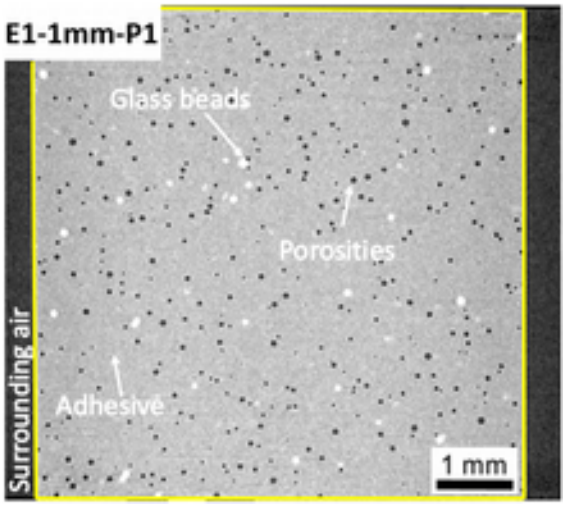

c) Reconstituted CT-scan in *x y* plane (sample E1)

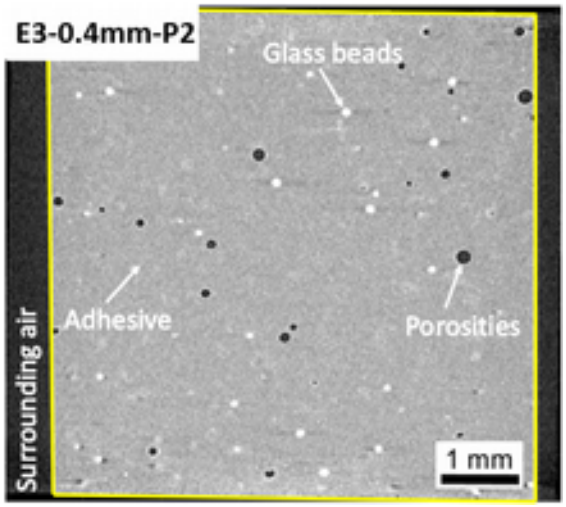

d) Reconstituted CT-scan in *x*y plane (sample E3)

Figure 7. Reconstituted volumes of the samples obtained from the CT scan

The air surrounding each sample was removed by detecting the effective contour of the sample (marked in yellow in Figure 7c and Figure 7d). This contour was identified for each image in the *xy* plane. Finally, the volume of sample E1 is composed of 227 images parallel to the *xy* plane, each image having a size of 1300 x 1400 pixels^2.

As for samples E2 and E3, the corresponding volumes contain respectively 103 and 86 images parallel to the *xy* plane, with the same size of 1300 x 1400 pixels^2.

The identification of the sample contour in each image was obtained using the Random Walks algorithm proposed in [21], which turns out to be very efficient in this case. Hence, the total volume occupied by the sample can be considered as the sum of all the pixels that are inside the contour of all the images. A mask can be then constructed for each image. In Figure 8b, the mask associated with the image shown in Figure 8a is presented. White pixels represent the volume of the sample and black pixels represent the area surrounding the sample.

The thresholds that allow the segmentation of phases in the sample volume are automatically detected using the Otsu algorithm [18]. Thus, a multi-threshold process is used with N_{thr}=3, aiming to discriminate the following phases: (i) pores, (ii) adhesive and (iii) glass beads. These multi-threshold values are obtained by maximizing the inter-class variance of grayscale levels for each class. To minimize the influence of the Charge-Coupled Device (CCD) sensor noise on the segmentation of each phase, a 3D median filter is applied to the complete raw volume. The filter size adopted here is of 3 x 3 x 3 voxels^3. The effect of the filter can be seen in Figure 8c when compared to the raw image shown in Figure 8a. Measurement of noise effect on the detection of pores or glass beads has been analyzed in-depth in [13], where the detection accuracy of pore volumes can go down to $1.8 \cdot 10^{-3}$%.

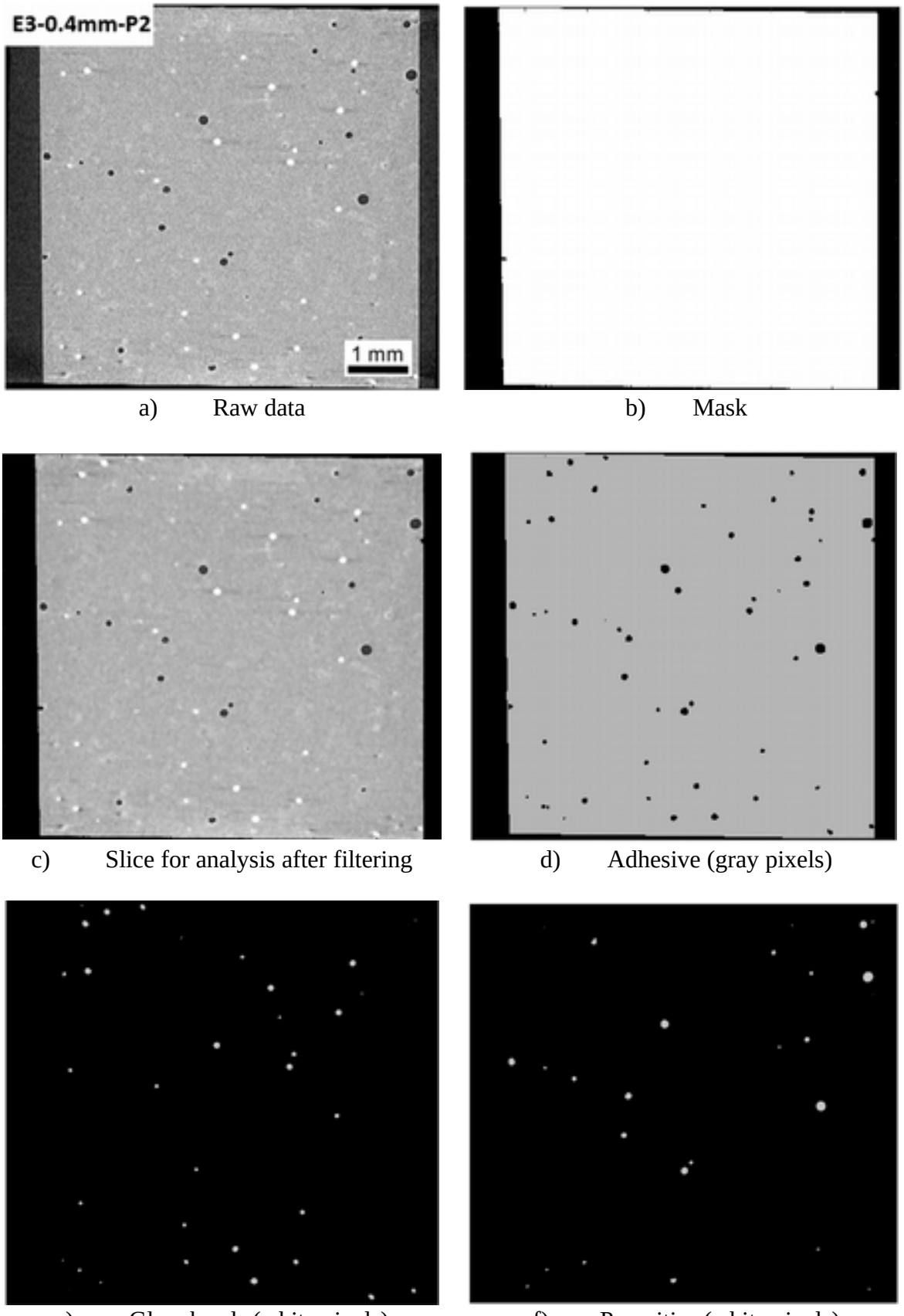

a) Raw data b) Mask

c) Slice for analysis after filtering d) Adhesive (gray pixels)

e) Glass beads (white pixels) f) Porosities (white pixels)

Figure 8. Results obtained from the segmentation of the phases in the adhesive

In Figure 8d, the adhesive phase is represented alone. The glass beads are shown in Figure 8e and the pores in Figure 8f. No pores or glass beads smaller than 3 voxels in diameter (13.5 µm) were considered in the analysis because the effect of CCD sensor noise on these features remains important despite the filtering used. At the end, all entities (pores or glass beads) for which the diameter is less than or equal to the size of the 3D median filter are excluded from the analysis.

3.3.3. Initial state of the adhesive

For an accurate understanding of the water absorption effect in adhesive materials, it is of great interest to know the microstructure, the distribution and the proportions of each phase at the initial state. The initial state can be referred to as the state of the adhesive immediately after curing. If the classical optical analysis with the KEYENCE VHX-7000 microscope was able to reveal the presence of each of these phases, the X-ray µ-tomography allowed us to determine quantitatively the different phases that compose the adhesive.

In Figure 9a, the spatial distribution of pores in sample E1 (with a thickness of 1 mm) is shown. A mostly homogeneous distribution is observed with some larger pores located close to the $\vec{y}$ axis. The origin of these pores could mostly be linked to the mixing process of component A and component B. In a direct manner, the process performed in atmospheric conditions could incorporate some air bubbles in the mix. Furthermore, the matrix contains glass beads, added by the manufacturer to ensure a minimum thickness during the bonding process in the case where the thickness of the adhesive is not imposed by specific elements. These glass beads could then be responsible for these larger porosities, as observed by Dumont *et al.* [19].

Figure 9c shows the pore distribution in sample E2. This distribution is mostly homogeneous and very similar to that of sample E1, despite the lower thickness of

about 0.4 mm. Besides, the distribution of pores in sample E3 has been represented in Figure 9e. The effect of vacuum on pore size and distribution is clearly visible. Few pores are observed and characterized by very large diameters. The distribution of glass beads within the samples E1, E2 and E3 is shown in Figure 9b, Figure 9d and Figure 9f, respectively. The glass beads have a rather spherical geometric shape. They are mostly solid, but hollow beads were also observed with a wall thickness between 20 µm and 30 µm.

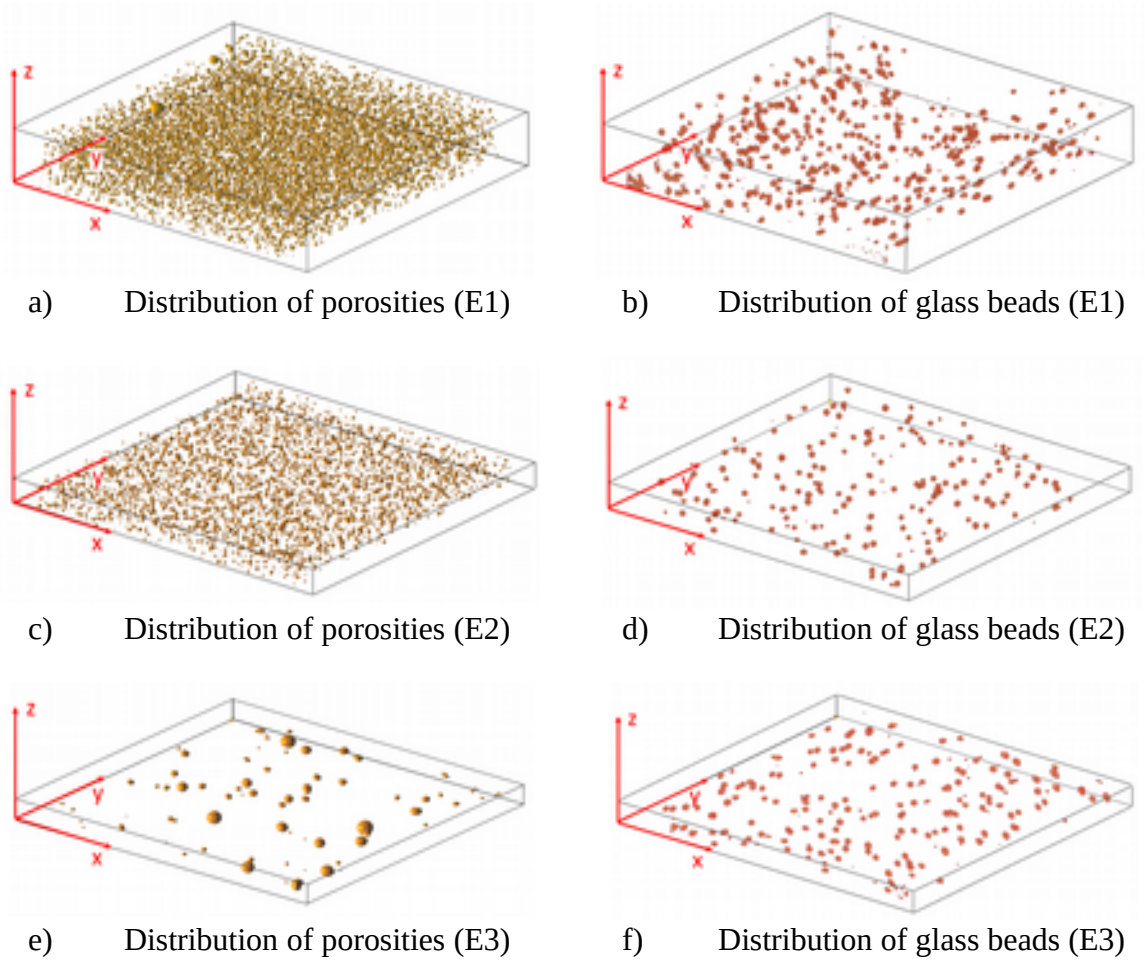

a) Distribution of porosities (E1) b) Distribution of glass beads (E1)

c) Distribution of porosities (E2) d) Distribution of glass beads (E2)

e) Distribution of porosities (E3) f) Distribution of glass beads (E3)

Figure 9. Distribution of the phases in the adhesive samples

The distribution of pores is plotted in Figure 10a versus their equivalent diameter for the three samples. The distribution is rather Gaussian for E1 and E2, with

equivalent diameters varying between 10 µm and 90 µm. More pores are detected for sample E1 than for E2, what was expected because of the larger thickness of sample E1, leading to a volume about 2.2 times greater.

Conversely, for sample E3, the distribution is mostly linear, with an equivalent diameter varying between 20 µm and 274 µm. The distribution of glass beads versus their equivalent diameter is shown in Figure 10b. The equivalent diameter of glass beads varies between 18 µm and 120 µm, with a similar trend for the three samples. More beads are detected in sample E1 again since its volume is larger.

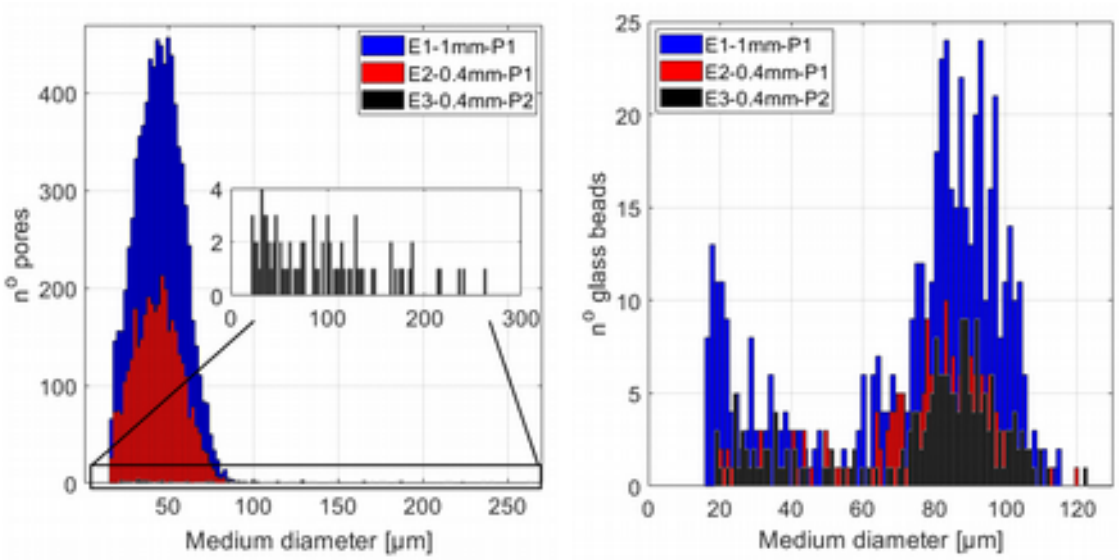

a) Pores b) Glass beads

Figure 10. Number of pores and glass beads in the samples

In order to further understand the differences between the three samples, the volume fraction of each phase was represented in Figure 11a for each of them. The porosity rate differs for the three samples. In the present case, porosity fractions of 1.54% and 1.37% were found, respectively for sample E1 and E2. Therefore, the thickness variation seems to influence the volumetric fraction of porosities, in the sense that the pore volume fraction increases with the thickness. In the literature [22-25], it has been shown that thicker joints had a lower breaking strength. This decrease in the

maximum breaking strength could find an explanation in the presence of pores with a greater density in thicker joints. In Figure 11a, it can also be seen that the effect of creating a vacuum on the adhesive, in the pasty state just after mixing, brings a significant improvement. The volume fraction of porosities is reduced from 1.37% for sample E2 (without vacuum) to 0.65% for sample E3 (with vacuum). Even though the overall porosity rate is much lower in sample E3, the presence of large pores can be very detrimental to the long-term mechanical strength of the adhesive joint. The volume fraction of glass beads is worth about 0.33% and is quasi-similar for the three samples. Furthermore, the numbers of pores and glass beads per unit volume are shown in Figure 11b. For sample E1, one finds 263 pores per mm^3 versus 255 pores per mm^3 for sample E2. In this way, the effect of thickness on the formation of pores can be hardly observed. In contrast, only 6 pores per mm^3 are found in sample E3. Besides, the density of glass beads is about 16 beads per mm^3, whatever the sample considered.

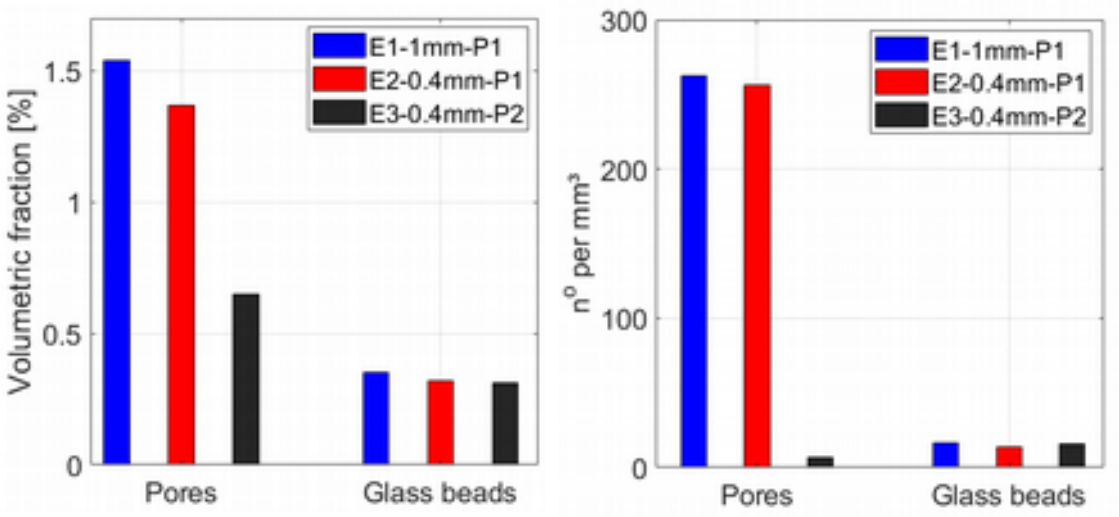

a) Pores/Glass beads volumetric fraction

b) Pores/Glass beads number per mm^3

Figure 11. Volume fractions and numbers of pores and glass beads in the different samples

In Figure 12, the real architecture of the reconstructed volume containing adhesive has been represented by eliminating the pores and excluding 1/8 of the volume in order to better visualize the adhesive phase inside the volume. The change in the effective section is a semi-local indicator that could provide relevant information about the compactness of the adhesive.

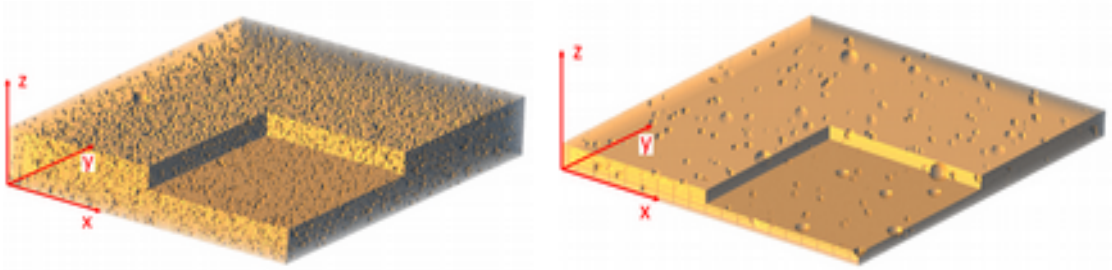

a) Effective volume of adhesive for sample E1

b) Effective volume of adhesive for sample E3

Figure 12. 3D representation of the effective volume of adhesive for samples E1 and E3

Figure 13 shows the three relative effective sections, according to the three directions of the reference frame displayed in Figure 12. These relative effective sections are obtained by using the following expressions:

$$S_x = \frac{S_{ex}}{S_{tx}} \tag{3}$$

$$S_y = \frac{S_{ey}}{S_{ty}} \tag{4}$$

$$S_z = \frac{S_{ez}}{S_{tz}} \tag{5}$$

where S_{ex}, S_{ey} and S_{ez} represent the effective sections in the $\vec{x}$, $\vec{y}$ and $\vec{z}$ directions, respectively. To determine S_{ex}, for instance, a section is carried out in the adhesive at a given value of x, with a plane perpendicular to the $\vec{x}$ axis (such a section is similar to the

one proposed in Figure 8d). S_{ex} is defined by the intersection of the plane with only the polymeric material (adhesive phase). S_{tx}, S_{ty} and S_{tz} represent the total section dimensions considered in the $\vec{x}$, $\vec{y}$ and $\vec{z}$ directions, respectively. To determine S_{tx}, a section is carried out in the adhesive as previously done, but all the phases are considered here in the determination of the intersection of the plane with the sample.

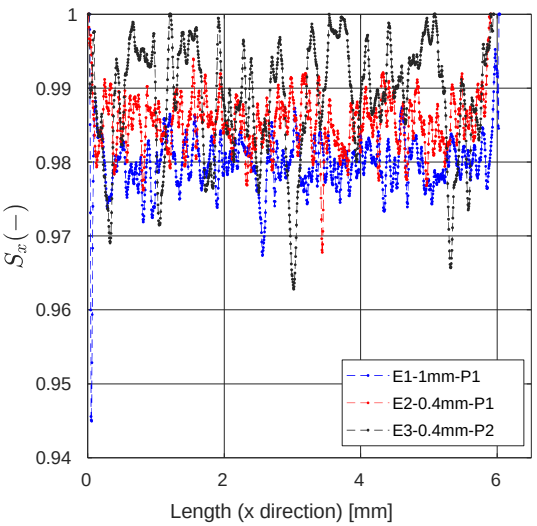

a) Effective section S_x in $\vec{x}$ direction

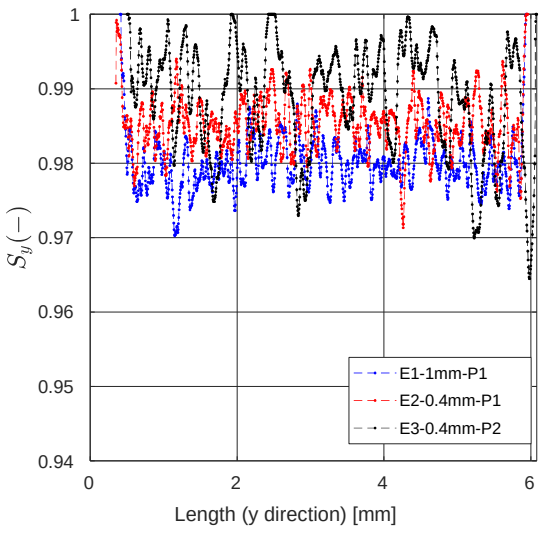

b) Effective section S_y in $\vec{y}$ direction

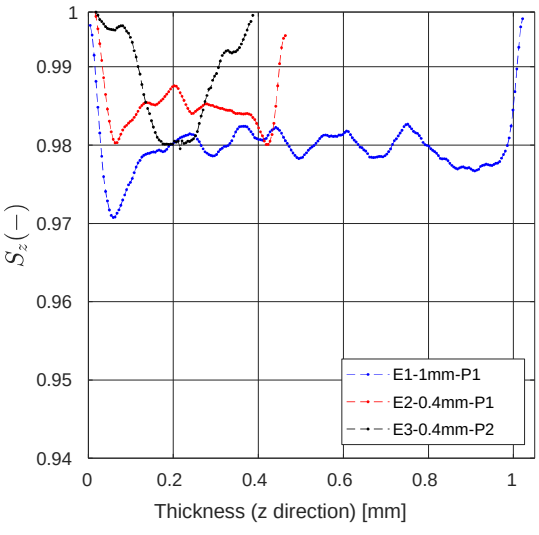

c) Effective section S_z in $\vec{z}$ direction

Figure 13. Evolution of the effective sections for the three samples

In Figure 13a, the evolution of the relative effective section S_x is plotted for the three samples. A rather homogeneous distribution in the $\vec{x}$ direction is observed for all three samples. The average value of each curve is very consistent with the associated porosity rate determined earlier. In samples E1 and E2, normal sections without any porosity (with S_x=1) are not observed. The range of variation of S_x is wider for sample E3. This is due to the fact that, locally, there may be relatively large porosities that could reduce the section S_x by almost 4% and, by contrast, there are also several sections with no porosities at all. The evolution of the relative effective section S_y is shown in Figure 13b, which turns out to be very similar to the previous one in the $\vec{x}$ direction. This means that the pore-type defects are uniformly distributed in sections perpendicular to the *xy* plane. On the contrary, in Figure 13c, significantly different evolutions are observed for the relative effective section S_z. Considering first samples E1 and E2, there is a sharp decrease/increase in S_z on the top/bottom surfaces, which indicates a significant localization of pores far from these surfaces. The explanation could be that, close to the two aluminum plates used, there is enough surface energy to "attract" the polymeric material, and the pores would be "pushed" towards the center of the joint. A similar evolution is observed for sample E3 where the largest pores are positioned in the middle of the joint, leading to a decrease/increase of 2% of the effective section for a variation of the through-thickness position of about 100 µm, located here at mid-thickness.

In addition to the previous analysis, the shape of the pore-type defects was thoroughly characterized by calculating their sphericity, which represents the level of similarity between the shape of an object and a sphere. The formula used here to calculate the sphericity was initially proposed by Wadell [26] and writes:

$$\psi = \frac{\pi^{\frac{1}{3}} \left(6 V_p\right)^{\frac{2}{3}}}{A_p} \tag{6}$$

where V_p and A_p represent the pore volume and surface area, respectively. The sphericity rate necessarily lies between 0 and 1. As an example, ψ is equal to 1 for a sphere, 0.806 for a cube, 0.874 for a cylinder and 0.671 for a tetrahedron.

In Figure 14, the sphericity distribution of the pores with respect to their equivalent diameter is plotted for the three different samples. It can be shown that most pores have a geometry close to a sphere. Only very few pores have a sphericity value below 0.6. These pores may result from the fusion of several pores and are characterized by a small equivalent diameter, often less than 20 µm, which gives rise to complex geometric shapes after voxelization.

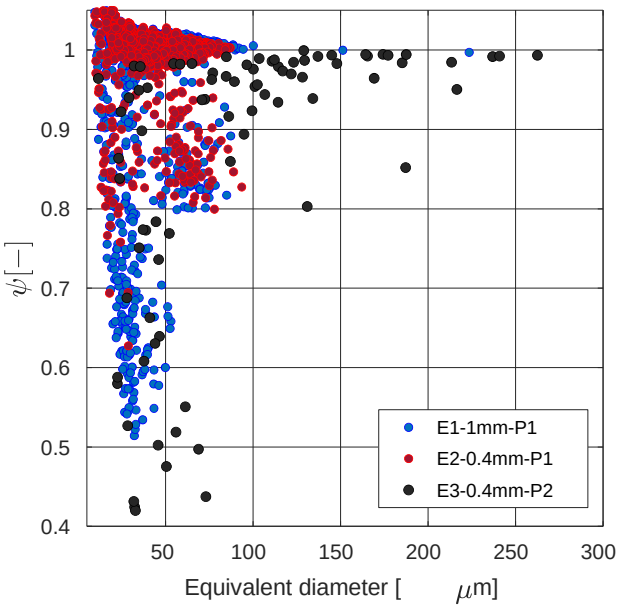

Figure 14. Sphericity of the pores

3.3.4. Water effect on the adhesive

Visualization of the waterfront. Dealing with water diffusion, several authors have been interested in the detection of the waterfront, particularly in heterogeneous media such as concrete, for example [11]. During diffusion, the water penetrates the material and may

change its density locally, allowing one to detect the presence of water by X-ray investigations.

In Figure 15, a cross-section of sample E3 is represented. This section is obtained by cutting the sample with a plane parallel to the *xz* plane at mid-distance between the edges (see Figure 7a). In order to get the visualization of the evolution of the water profile, this section is represented for eight successive aging times between the initial state (0 days) and a final state, 4 months later (120 days). Unfortunately, the waterfront within the sample, which should have been located through a variation of gray levels in the normal direction to the sample surface, is not detected here. Several reasons are likely to explain that.

First, the water is supposed to fill the free volume of the sample by capillarity. The free volume is the difference between the total macroscopic volume of the sample and that actually occupied by the molecules that constitute it. This free volume is localized between the chains of molecules [27] with a characteristic size lower than a micrometer and does not represent, in any case, the porosities. Hence, if this scenario occurs, the volume change should not be detected during the water uptake until this free volume is completely filled. That being said, it can be noticed in Figure 15 that the width of sample E3, denoted as l_0 at the initial state, slightly changes from 5 days of immersion, becoming then l_i. This variation in size is certainly due to hydric swelling. Most of all, if the pores end up filling with water (whereas the glass beads remain quasi-unchanged), the water occupying the pores displays a gray level almost identical to the one of the adhesive phase, due to the closeness of the respective densities of the demineralized water and the adhesive.

Figure 16 depicts the same observations performed on a section of sample E1 for similar aging times. Although this sample is 1 mm thick, no variation in gray level has

been detected either, which could represent the water profile in the sample. However, the pore filling is more visible, especially in the vicinity of the faces normal to the $\vec{z}$ direction. As for the glass beads, they do not present a detectable evolution, keeping their diameters virtually constant. Some artifacts are also visible on the beads near the left edge.

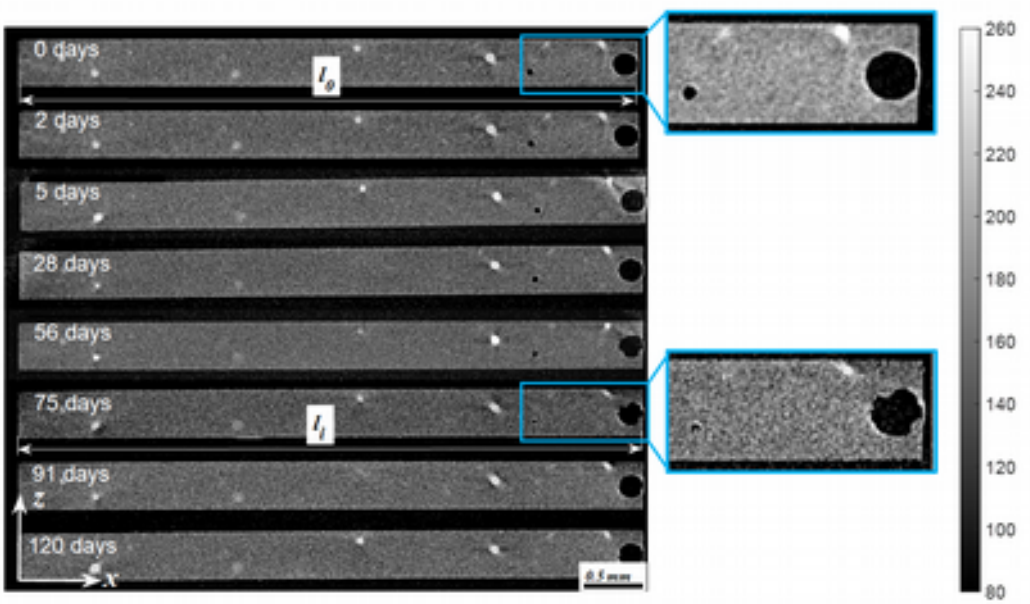

Figure 15. Gray levels in sample E3 versus aging time

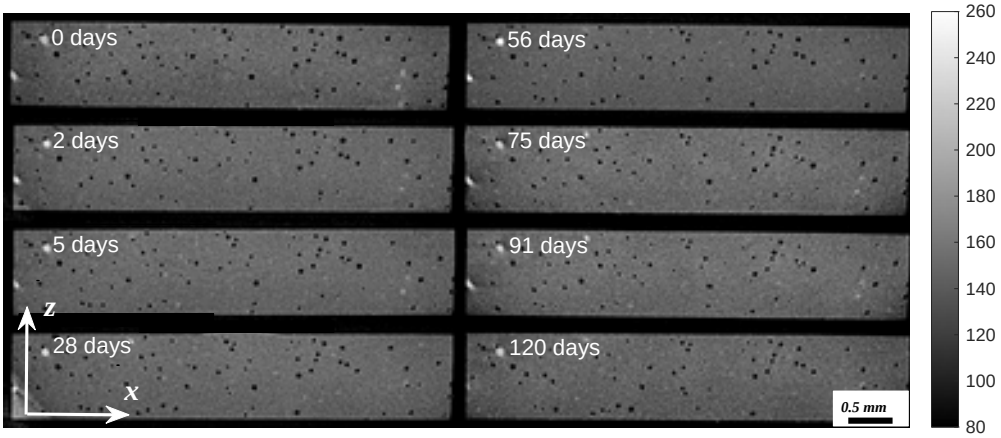

Figure 16. Gray levels in sample E1 versus aging time

In order to further analyze the pore filling, a section in the *xy* plane was performed at a distance of 54 µm from the surface of sample E2. Figure 17 shows the

filling evolution at this section between the initial state (Figure 17a) and after 28 days (Figure 17b). The pores seem to shrink considerably and change their geometric shape due to the water that occupies their volumes.

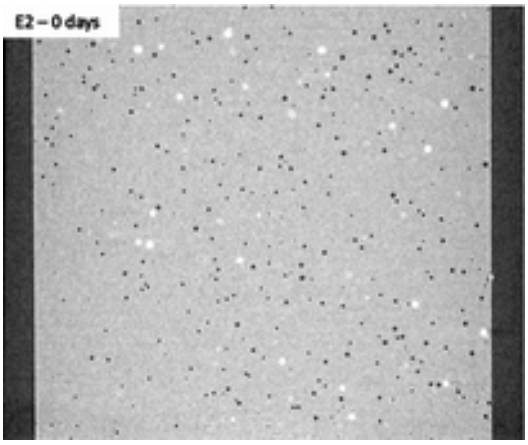

a) Initial section located at 54 µm depth in the thickness ($\vec{z}$ direction)

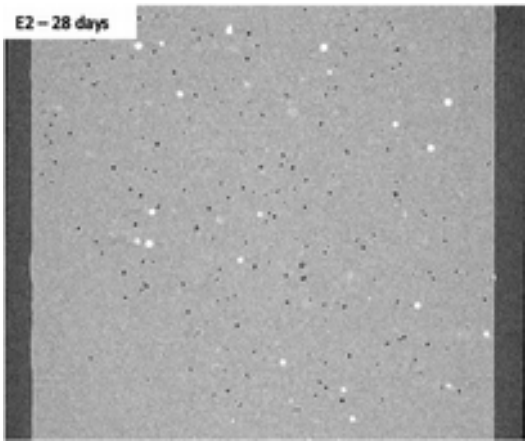

b) Section after 28 days taken at 54 µm depth in the thickness ($\vec{z}$ direction)

Figure 17. Sections in sample E2 illustrating the pore filling

Evolution of volume ratios of adhesive, pores and glass beads. Despite the fact that one cannot detect the evolution of the waterfront in the samples, it is however possible to determine the evolution of each phase constituting the adhesive material in terms of volume ratio. First of all, the evolution with the aging time of the volume with a density (gray scale) close to that of the polymeric material or water is investigated. This volume change is calculated as follows:

$$\Delta V_a(\%) = \frac{V_{adh(t)} - V_{adh0}}{V_{adh0}} \times 100 \tag{7}$$

where $V_{adh(t)}$ represents the polymer and water volume for an aging time *t*, and V_{adh0} the polymer and water volume in the initial state. At each time *t*, the polymer and water volume $V_{adh(t)}$ is determined as the difference between the total volume of the sample $V_{total(t)}$ and both the volume of glass beads $V_{beads(t)}$ and the pore volume $V_{pores(t)}$:

$$V_{adh(t)} = V_{total(t)} - V_{beads(t)} - V_{pores(t)} \tag{8}$$

The volumetric fractions of pores and beads are determined using the following expressions:

$$\Delta V_p(\%) = \frac{V_{pores(t)} - V_{pores0}}{V_{adh0}} \times 100 \quad (9)$$

$$\Delta V_b(\%) = \frac{V_{beads(t)} - V_{beads0}}{V_{adh0}} \times 100 \quad (10)$$

where $V_{pores(t)}$ and $V_{beads(t)}$ represent respectively the pore and bead volumes at an aging time *t*, and V_{pores0} and V_{beads0} represent the same volumes at the initial state.

Figure 18a displays the relative evolution of the polymer and water volume ΔV_a for each sample as a function of the square root of time normalized by the sample thickness. This representation is similar to the one depicted in Figure 5. This evolution in volume should be correlated with the variation of mass mentioned previously. However, a slight shift is observed between these two quantities, as will be discussed later.

In Figure 18b, the evolution of the porosity fraction ΔV_p is represented, again as a function of the square root of time divided by the sample thickness. For sample E1, a first regime is observed during which the global pore volume remains quasi-constant, followed by a slow decrease from $2 \times 10^6 \frac{\sqrt{s}}{m}$. This reduction may be attributed to the filling of pores with water, which starts in the pores closest to the sample free surfaces and gradually evolves towards the center of the sample. A similar behavior is observed with sample E2, for which the first regime ends around $1 \times 10^6 \frac{\sqrt{s}}{m}$ with a very slight decrease. In both cases of samples E1 and E2, the second regime allows one to determine the pore filling speed when the sample is immersed in water. For sample E3,

the first regime ends at nearly $3 \times 10^6 \frac{\sqrt{s}}{m}$. This first regime seems to be influenced as much by the joint thickness as by the size and spatial distribution of pores. If the first regime ends so late, it is probably due to the quite significant average distance between the free surfaces of the sample (normal to $\vec{z}$) and the first closest pores. Owing to the relatively large size of pores in this sample, they are found to be located more at mid-thickness than close to the free surfaces. Moreover, the average distance between pores (still significant in sample E3) could also be a factor influencing the pore filling start time.

Figure 18c presents the evolution of the volumetric fraction of glass beads ΔV_b. The three samples show a quasi-constant volumetric fraction of glass beads during the entire measurement period, which suggests that water does not penetrate the beads, as naturally expected. By the way, these results enhance the robustness of the image processing method and enable one to ensure that the volumes investigated are representative with respect to the phases analyzed.

Further understanding of the correlation between the polymer and water volume change ΔV_a and the mass change C was achieved by plotting their relative dependence in Figure 19. It can be observed, at the initial stage of water absorption, that the mass of the samples increases without detecting a variation in volume. This phenomenon may be explained by the fact that water penetrates the sample in filling first some free volumes by capillarity. Once these free volumes are filled, a linear dependence between the mass of the samples and their volume is observed. This pattern is in perfect agreement with previous works in the literature (see [28], for instance).

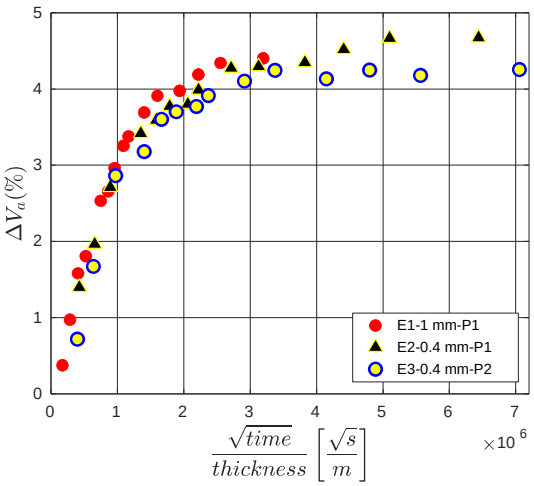

a) Evolution of polymer and water volume versus aging time

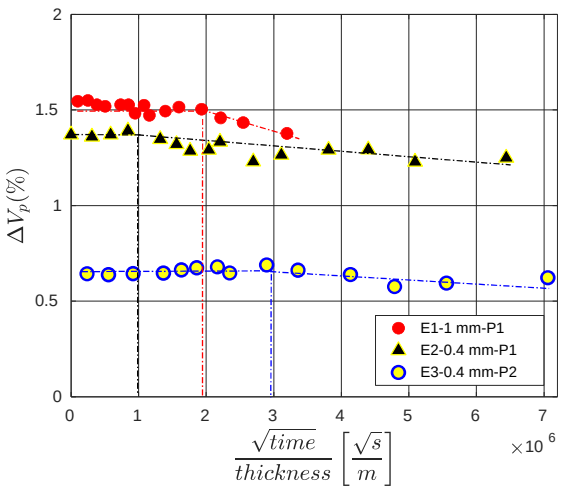

b) Evolution of the volumetric fraction of pores versus aging time

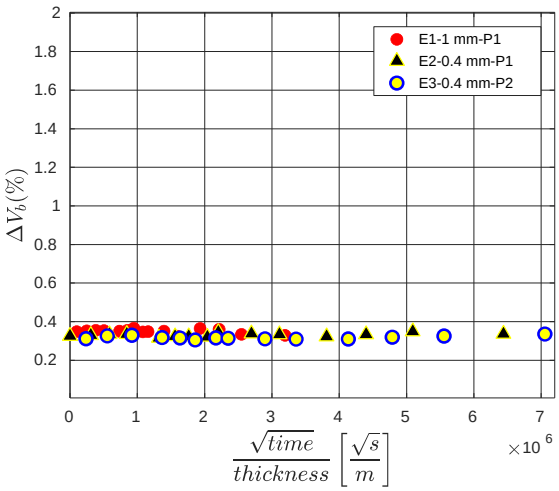

c) Evolution of the volumetric fraction of glass beads versus aging time

Figure 18. Evolution of the different phases of the adhesive material

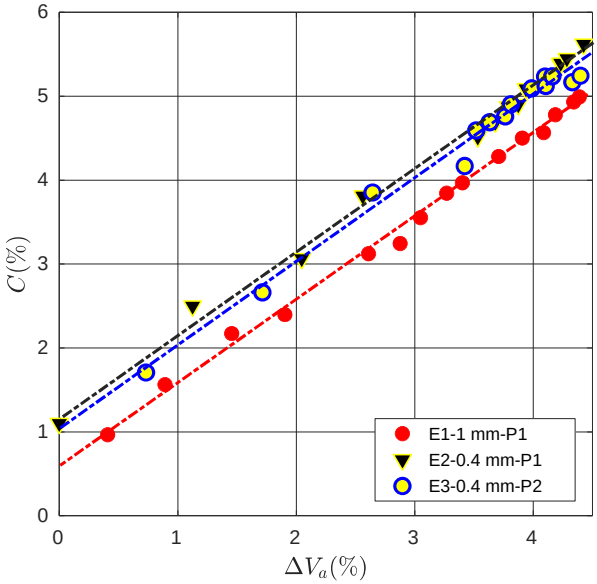

Figure 19. Mass change of the samples versus variation in the effective volume of the adhesive

Sphericity of the pores. The water which penetrates the pores modifies considerably their geometry. The relevant parameter to characterize the geometric shape of the pores during water aging is again the sphericity. In Figure 20, the sphericity distribution of pores in sample E2 is represented at four aging times (including the initial state) with respect to their equivalent diameter.

As formerly observed in Figure 14, most of the pores have initially a quite spherical shape, but with a large variety of diameters. Only few pores (whose diameter is around 20 µm) have a sphericity index lower than 0.8. Such pores are mainly close to the free surfaces of the sample and have been generated by the waterjet cutting, or these are small pores which must certainly have merged during the curing cycle. The sphericity of pores after 5 days of immersion is shown in Figure 20b. For most of them, there is no relevant change in the geometric shape, except for some characterized by an equivalent diameter between 20 µm and 30 µm. As said before, such pores of small diameter are generally located near the free surfaces and water naturally begins to penetrate them, leading thus to a decrease of their sphericity. Bigger pores also localized

not far from the edges may also fill up with water. However, at this time, the amount of water brought into play is very small when compared to the size of the larger pores and it does not result in any significant change of their shape, unlike smaller ones. After 28 days of water aging, it is observed that the geometric shape of a considerable proportion of pores is affected. As previously noted, the lowest sphericity level is obtained with the smallest pores, reducing down to 0.55. However, water begins to modify significantly the sphericity of pores of intermediate diameters. At this aging time, an average decrease in sphericity from 1 to 0.92 is observed for pores between 30 µm and 70 µm, with a maximum change for pores between 45 µm and 50 µm. This decrease in sphericity can be further visualized in Figure 20d, where it is obvious that the larger pores are also affected by water penetration. In Figure 20d, it is even possible to notice a separation between two regions, a first one where the pores are not yet affected by water (with a sphericity close to 1), and a second one where sphericity has dropped down to 0.9 at the minimum, due to the increasing amount of water in the material. The comparison between the initial and final states is also represented in Figure 21 in a different manner.

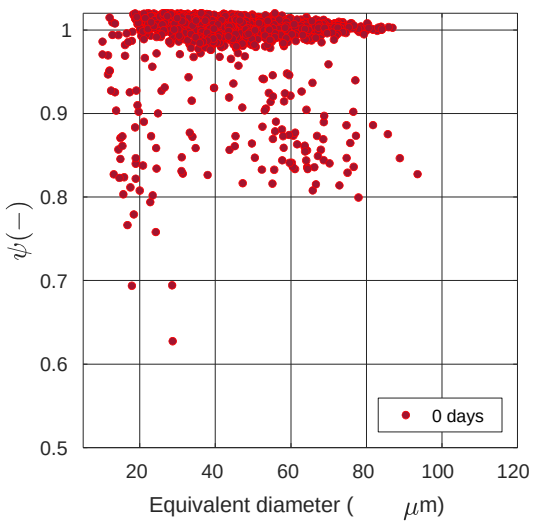

a) Sphericity distribution at the initial state

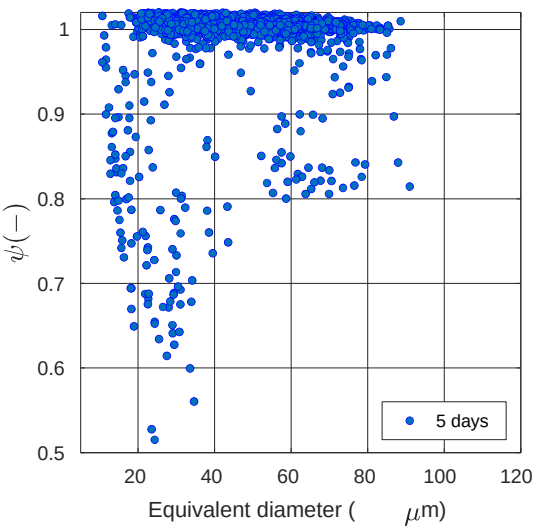

b) Sphericity distribution after 5 days of immersion

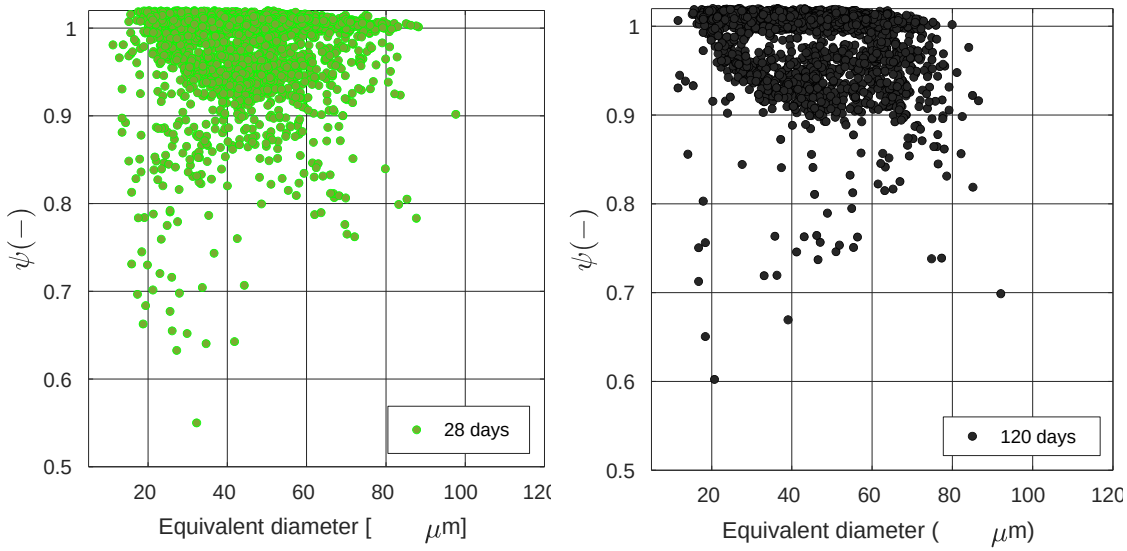

c) Sphericity distribution after 28 days of immersion

d) Sphericity distribution after 120 days of immersion

Figure 20. Evolution of the sphericity distribution of pores with aging time for sample E2

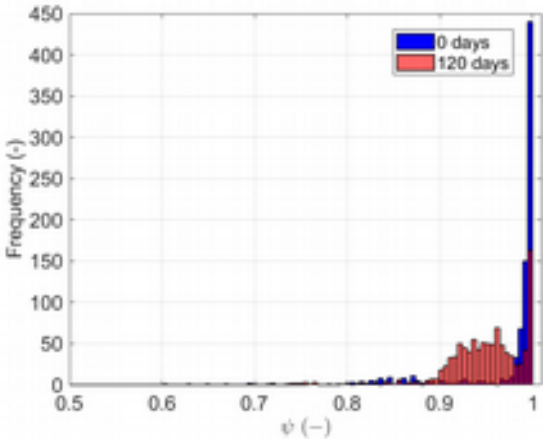

Figure 21. Evolution of the sphericity distribution of pores in terms of frequency

Local distribution of water in the pores. A straightforward way to better understand the evolution of pore filling in a preferential direction (along the thickness of the samples, for example), when the sample is immersed in water, amounts to studying the evolution of the pore sections. Figure 22 depicts the global area S_{pores} occupied by the pores (in pixels^2), for several sections in the *xy* plane at different positions along the thickness.

The parameter w_s represents the effective thickness of the sample. As formerly shown, between the free surfaces of the sample and the first pores, there is a slice of adhesive with a thickness w_m varying between 12 µm and 25 µm (depending on the process and the sample), in which no pores are present.

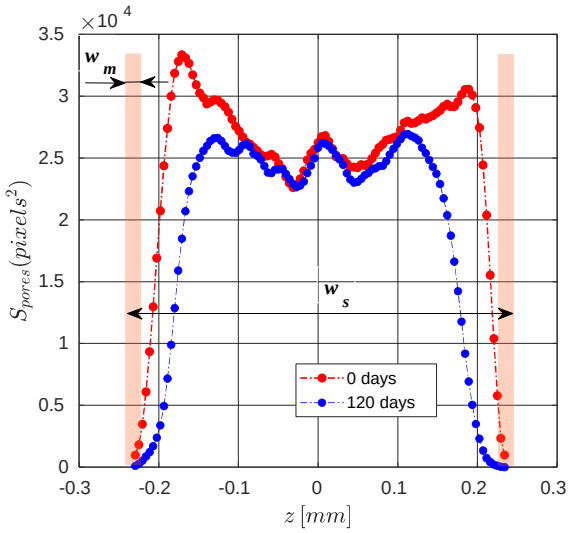

Figure 22. Evolution of the pore sections along the thickness direction in sample E2, at the initial state and after 120 days of aging

At the initial state, the variation of the pore section along the thickness of the sample is quite consistent with the porosity profile according to the $\vec{z}$ direction represented in Figure 13c, with two peaks of pore concentration in the vicinity of the two free surfaces normal to the $\vec{z}$ axis. Then, the water effect on the evolution of these pore sections is clearly visible. A significant decrease is particularly observed around the free surfaces between the initial state and the final state after 120 days of immersion. Therefore, this evolution only concerns the areas with high pore concentration, i.e. for z varying between +/- 0.2 mm and +/- 0.1 mm. Conversely, almost no changes occur in the central part of the sample, i.e. for z in the interval [-0.1 mm, 0.1 mm].

The filling percentage of the initial pore sections, determined from the section evolution, is calculated with the following expression:

$$C_{local\,p/p}(\%) = \frac{S_{pores(0)} - S_{pores(t)}}{S_{pores(0)}} \times 100 \quad (11)$$

This analysis is performed in each section at a whole and does not provide a filling value for each pore individually. This pore filling percentage $C_{local\,p/p}$ is plotted in Figure 23a. It is observed that, after only 5 days, the first sections tangent to the first pores are affected by the presence of water, even if it is not possible to clearly detect any water droplets at the local scale (probably because of the insignificant amount of water existing in the pores). After 28 days of immersion, the first pores closest to the free surfaces are filled to an average amount of 80%. At this time, it is also noticed that the first pores in which water is detected are found to lie at about 65 µm from the corresponding external surface. After 120 days, the pores closest to the free surfaces are almost totally filled (with a percentage of water close to 100%) and the area along the $\vec{z}$ direction in which water is detected is about 130 µm thick.

Furthermore, the average percentage of water in the pores, related to the initial entire section area of the adhesive $S_{tz(0)}$, has been determined using the following expression, for each successive section in the $\vec{z}$ direction:

$$C_{local\,p/a}(\%) = \frac{S_{pores(0)} - S_{pores(t)}}{S_{tz(0)}} \times 100 \quad (12)$$

Figure 23b displays this water percentage $C_{local\,p/a}$ in the pores. It can be observed that the two areas where the pores are almost filled (after 120 days) show a global percentage of water equal to 1.4% at the maximum on the left side and 1.76% on the right side, respectively. This dissymmetry should naturally be correlated with the pore concentration which is slightly higher on the right side.

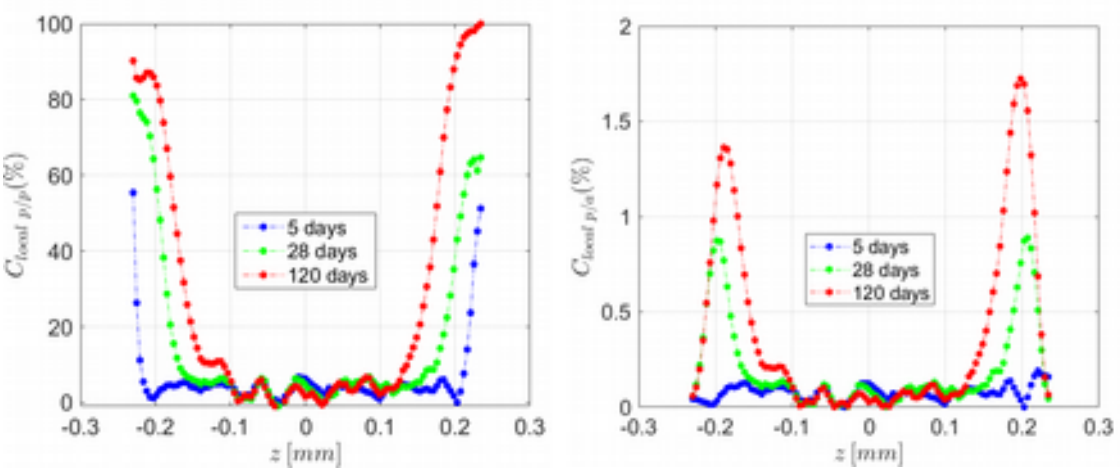

a) Percentage of water in pores related to the section area of pores

b) Percentage of water in pores related to the entire section area of adhesive

Figure 23. Evolution of water proportion in pores along the $\vec{z}$ direction in sample E2

All these results show that a tomographic analysis allows one to characterize the water uptake inside an adhesive material with a very good accuracy. The evolution of the waterfronts shall be deduced from the evolution of the volumes of the pores within the adhesive. Then, these evolutions will provide relevant information on the kinetics of water uptake, allowing one to tend more judiciously towards an optimal diffusion model.

4. Conclusions and perspectives

This paper presents an investigation on the mechanisms of water uptake in a bi-component epoxy structural adhesive by using X-ray µ-tomography (a non-contact and therefore non-intrusive technique), by measuring weight variations, and by performing microscopic analyses. At the initial state, the adhesive joint is heterogeneous and also displays a population of pore-type defects. These porosities are mainly generated during the mixing process between the two components of the adhesive. The curing cycle may contribute additionally to the creation of pores, but it remains relatively inconsequential, due to the low cure temperature in the present study. The number of porosities highly

increases with the thickness of the adhesive specimen, which weakens its effective section. Concerning the initial state, it has been finally shown that no pores appear near the free surfaces of the samples (at the interface with the substrates in the bonded assembly) with a minimal distance between these surfaces and the first pores varying between 15 µm and 20 µm.

Dealing now with water uptake, attempts were made to measure the waterfront and thus the filling speed throughout the adhesive material. Unfortunately, water could not be identified separately from the adhesive material, due to the proximity between the polymer and water densities. Weight and volume measurements allowed one, however, to rule on the course of events. The water that penetrates the adhesive fills in first the free volume of the material by capillarity and then, the absorbed quantity of water is found almost entirely in the volume of pores. The dependence relationship between the mass and volume of samples is quasi-linear, with a shift upon the beginning of aging corresponding to the filling of the free volume. The occurrence of water in the shape of droplets inside the pores has then been detected, first qualitatively by microscopic observations, and then quantitatively by tomographic investigations. Finally, the evolution of the pore filling front may alternatively contribute to a judicious choice of a water diffusion model.

This work opens up a number of perspectives. Primarily, the proportionality between the change in mass and the change in volume of the adhesive is probably related to the affinity of water with the adhesive. This aspect associates the diffusion of water within the polymer with the presence of polar chemical groups. These groups have the capacity to create hydrogen bonds with the water molecules, which increases the global volume of the material. Hydroxyl or amine groups, found in most epoxy resins or epoxy adhesives, are highly hydrophilic. The dependence between mass and

volume could also enable the determination of a swelling coefficient. Next, the definition and prediction of swell is interesting with the idea of estimating its effect on the distribution of mechanical stresses within the adhesive during water aging. Subsequently, all these tomographic observations, when performed during sorption/desorption cycles, may show the irreversibility and the damage that an adhesive joint could suffer during the cycling of water aging.

Acknowledgements

The authors are indebted to the DGA (Direction Générale de l'Armement) for its financial support.

Declaration of competing interest

The authors declare that they have no known competing financial interests or personal relationships that could have appeared to influence the work reported in this paper.

References

[1] N. Leconte, B. Bourel, F. Lauro, C. Badulescu, and E. Markiewicz, "Strength and failure of an aluminum/PA66 self-piercing riveted assembly at low and moderate loading rates: Experiments and modeling," *Int. J. Impact Eng.*, vol. 142, p. 103587, 2020, doi: https://doi.org/10.1016/j.ijimpeng.2020.103587.

[2] C. Badulescu, J. Y. Cognard, R. Créac'hcadec, and P. Vedrine, "Analysis of the low temperature-dependent behaviour of a ductile adhesive under monotonic tensile/compression-shear loads," *Int. J. Adhes. Adhes.*, vol. 36, pp. 56–64, 2012, doi: 10.1016/j.ijadhadh.2012.03.009.

[3] A. Ilioni, P. Y. Le Gac, C. Badulescu, D. Thevenet, and P. Davies, “Prediction of Mechanical Behaviour of a Bulk Epoxy Adhesive in a Marine Environment,” *J. Adhes.*, vol. 95, pp. 1–21, 2018, doi: 10.1080/00218464.2017.1377616.

[4] A. Ilioni, C. Badulescu, N. Carrere, P. Davies, and D. Thévenet, “A viscoelastic-viscoplastic model to describe creep and strain rate effects on the mechanical behaviour of adhesively-bonded assemblies,” *Int. J. Adhes. Adhes.*, vol. 82, 2017, pp. 184–195, 2018, doi: 10.1016/j.ijadhadh.2017.12.003.

[5] A. Toscano, G. Pitarresi, M. Scafidi, M. Di Filippo, G. Spadaro, and S. Alessi, “Water diffusion and swelling stresses in highly crosslinked epoxy matrices,” *Polym. Degrad. Stab.*, vol. 133, pp. 255–263, 2016, doi: https://doi.org/10.1016/j.polymdegradstab.2016.09.004.

[6] P. P. Selakjani, A. Dorieh, A. Pizzi, M. H. Shahavi, A. Hasankhah, S. Shekarsaraee, M. Ashouri, and S. G. Movahed, “Reducing free formaldehyde emission, improvement of thickness swelling and increasing storage stability of novel medium density fiberboard by urea-formaldehyde adhesive modified by phenol derivatives,” *Int. J. Adhes. Adhes.*, vol. 111, p. 102962, 2021, doi: https://doi.org/10.1016/j.ijadhadh.2021.102962.

[7] R. Oliveira, L. Bilro, T. H. R. Marques, C. M. B. Cordeiro, and R. Nogueira, “Simultaneous detection of humidity and temperature through an adhesive based Fabry–Pérot cavity combined with polymer fiber Bragg grating,” *Opt. Lasers Eng.*, vol. 114, pp. 37–43, 2019, doi: https://doi.org/10.1016/j.optlaseng.2018.10.007.

[8] R. Grangeat, M. Girard, C. Lupi, D. Leduc, and F. Jacquemin, “Measurement of the local water content of an epoxy adhesive by fiber optic sensor based on Fresnel reflection,” *Mech. Syst. Signal Process.*, vol. 141, p. 106439, 2020, doi:

https://doi.org/10.1016/j.ymssp.2019.106439.

[9] A. Bridarolli, M. Odlyha, G. Burca, J. C. Duncan, F. A. Akeroyd, A. Church, and L. Bozec, “Controlled environment neutron radiography of moisture sorption/desorption in nanocellulose-treated cotton painting canvases,” *ACS Appl. Polym. Mater.*, vol. 3, no. 2, pp. 777–788, 2021, doi: 10.1021/acsapm.0c01073.

[10] J. Dewanckele, T. De Kock, G. Fronteau, H. Derluyn, P. Vontobel, M. Dierick, L. Van Hoorebeke, P. Jacobs, and V. Cnudde, “Neutron radiography and X-ray computed tomography for quantifying weathering and water uptake processes inside porous limestone used as building material,” *Mater. Charact.*, vol. 88, pp. 86–99, 2014, doi: https://doi.org/10.1016/j.matchar.2013.12.007.

[11] B. Van Belleghem, R. Montoya, J. Dewanckele, N. Van den Steen, I. De Graeve, J. Deconinck, V. Cnudde, K. Van Tittelboom, and N. De Belie, “Capillary water absorption in cracked and uncracked mortar – A comparison between experimental study and finite element analysis,” *Constr. Build. Mater.*, vol. 110, pp. 154–162, 2016, doi: https://doi.org/10.1016/j.conbuildmat.2016.02.027.

[12] V. Dumont, C. Badulescu, G. Stamoulis, J. Adrien, E. Maire, A. Lefèvre, and D. Thévenet, “On the influence of mechanical loadings on the porosities of structural epoxy adhesives joints by means of in-situ X-ray microtomography,” *Int. J. Adhes. Adhes.*, vol. 99, pp. 102568-1–102568-14, 2020, doi: 10.1016/j.ijadhadh.2020.102568.

[13] V. Dumont, C. Badulescu, J. Adrien, N. Carrere, D. Thévenet, and E. Maire, “Experimental investigation of porosities evolution in a bonded assembly by means of X-ray tomography,” *J. Adhes.*, vol. 97, no. 6, pp. 528–552, 2021, doi: 10.1080/00218464.2019.1685984.

[14] M. Deroiné, A. Le Duigou, Y. M. Corre, P. Y. Le Gac, P. Davies, G. César, and S. Bruzaud, “Accelerated ageing of polylactide in aqueous environments: Comparative study between distilled water and seawater,” *Polym. Degrad. Stab.*, vol. 108, pp. 319–329, 2014, doi: https://doi.org/10.1016/j.polymdegradstab.2014.01.020.

[15] B. Pollak, “ Experiences with planography from the Fort William Sanatorium, Fort William, Ontario, Canada ” *Dis. Chest*, vol. 24, no. 6, pp. 663–669, 1953, doi: https://doi.org/10.1378/chest.24.6.663.

[16] M. Sezgin and B. Sankur, “Survey over image thresholding techniques and quantitative performance evaluation,” *J. Electron. Imaging*, vol. 13, no. 1, pp. 146–165, 2004, doi: 10.1117/1.1631315.

[17] A. Rosenfeld and P. D. La Torre, “Histogram concavity analysis as an aid in threshold selection,” *IEEE Trans. Syst. Man. Cybern.*, vol. SMC-13, no. 2, pp. 231–235, 1983, doi: 10.1109/TSMC.1983.6313118.

[18] N. Otsu, “A Threshold Selection Method from Gray-Level Histograms,” *IEEE Trans. Syst. Man Cybern.*, vol. 9, no. 1, pp. 62–66, 1979, doi: 10.1109/tsmc.1979.4310076.

[19] V. Dumont, C. Badulescu, G. Stamoulis, J. Adrien, E. Maire, A. Lefèvre, and D. Thévenet, “On the effect of the curing cycle on the creation of pores in structural adhesive joints by means of X-ray microtomography,” *J. Adhes.*, vol. 97, no. 12, pp. 1073–1106, 2021, doi: 10.1080/00218464.2020.1728257.

[20] J. Schindelin *et al.*, “Fiji: an open-source platform for biological-image analysis,” *Nat. Methods*, vol. 9, no. 7, pp. 676–682, 2012, doi: 10.1038/nmeth.2019.

[21] L. Grady, “Random walks for image segmentation,” *IEEE Trans. Pattern Anal. Mach. Intell.*, vol. 28, no. 11, pp. 1768–1783, 2006, doi:

10.1109/TPAMI.2006.233.

[22] D. M. Gleich, M. J. L. Van Tooren, and A. Beukers, “Analysis and evaluation of bondline thickness effects on failure load in adhesively bonded structures,” *J. Adhes. Sci. Technol.*, vol. 15, no. 9, pp. 1091–1101, 2001, doi: 10.1163/156856101317035503.

[23] L. F. M. da Silva, T. N. S. S. Rodrigues, M. A. V Figueiredo, M. F. S. F. de Moura, and J. A. G. Chousal, “Effect of Adhesive Type and Thickness on the Lap Shear Strength,” *J. Adhes.*, vol. 82, no. 11, pp. 1091–1115, 2006, doi: 10.1080/00218460600948511.

[24] H. Chai, “The effects of bond thickness, rate and temperature on the deformation and fracture of structural adhesives under shear loading,” *Int. J. Fract.*, vol. 130, no. 1, pp. 497–515, 2004, doi: 10.1023/B:FRAC.0000049504.51847.2a.

[25] R. J. C. Carbas, M. A. Dantas, E. A. S. Marques, and L. F. M. da Silva, “Effect of the adhesive thickness on butt adhesive joints under torsional loads,” *J. Adv. Join. Process.*, vol. 3, p. 100061, 2021, doi: https://doi.org/10.1016/j.jajp.2021.100061.

[26] H. Wadell, “Volume, Shape, and Roundness of Quartz Particles,” *J. Geol.*, vol. 43, pp. 250–280, May 1935, doi: 10.1086/624298.

[27] C. Chen, B. Han, J. Li, T. Shang, J. Zou, and W. Jiang, “A new model on the diffusion of small molecule penetrants in dense polymer membranes,” *J. Memb. Sci.*, vol. 187, no. 1, pp. 109–118, 2001, doi: https://doi.org/10.1016/S0376-7388(00)00689-X.

[28] M. J. Adamson, “Thermal expansion and swelling of cured epoxy resin used in graphite/epoxy composite materials,” *J. Mater. Sci.*, vol. 15, no. 7, pp. 1736–1745, 1980, doi: 10.1007/BF00550593.